Texture-Based Optimization of Crystal Plasticity Parameters: Application to Zinc and Its Alloy

KAROL FRYDRYCH, ANNA JARZĘBSKA, SAKETH VIRUPAKSHI, KATARZYNA KOWALCZYK-GAJEWSKA, MAGDALENA BIEDA, ROBERT CHULIST, MONIKA SKORUPSKA, NORBERT SCHELL, and KRZYSZTOF SZTWIERTNIA

Evolutionary algorithms have become an extensively used tool for identification of crystal plasticity parameters of hexagonal close packed metals and alloys. However, the fitness functions were usually built using the experimentally measured stress–strain curves. Here, the fitness function is built by means of numerical comparison of the simulated and experimental textures. Namely, the normalized texture difference index is minimized. The evolutionary algorithm with the newly developed fitness function is tested by performing crystal plasticity parameter optimization for both pure zinc and zinc-magnesium alloy. These materials are promising candidates for bioabsorbable implants due to good biocompatibility and optimal corrosion rate. Although their mechanical properties in the as-cast state do not fulfill the requirements, they can be increased by means of hydrostatic extrusion. The developed modeling approach enabled acquisition of the crystal plasticity parameters and analysis of the active deformation mechanisms in zinc and zinc-magnesium alloy subjected to hydrostatic extrusion. It was shown that although slip systems are the main deformation carrier, compressive twinning plays an important role in texture evolution. However, the texture is also partially affected by dynamic recrystallization which is not considered within the developed framework.

I. INTRODUCTION

THE macroscopic properties of metallic materials are related to their microstructure, in particular in the case of plastic behavior. However, understanding this relationship is not trivial, especially in the case of the hexagonal close packed (HCP) metals, with many potential slip and twinning systems. The crystal plasticity (CP) theory offers great help in this task. Among HCP metals, the particular attention was recently paid to titanium[1,2] and magnesium[3–5] due to their high specific strength. Also zirconium (*cf. e.g.*,[6,7]) was studied extensively thanks to its application as fuel cladding in nuclear power plants.

On the other hand, HCP zinc and its alloys received considerably less attention. However, they are important industrial materials, as steel elements are often coated with zinc for protection against corrosion. It should be also noted that good biocompatibility and optimal corrosion rate have made zinc and its alloys promising candidates for producing bioabsorbable implants *e.g.*, stents.[8,9] Such implants should dissolve gradually in the physiological environment after fulfilling their mission to support damaged tissue during its recovery process. Furthermore, generated corrosion products need to be safely metabolized by human body without any harmful response. Temporary implants could prevent patients from chronic inflammatory, thrombogenicity and endothelial dysfunction. The main disadvantage of zinc and its alloys, limiting their applications for those purposes are low mechanical properties, in particular the yield strength, ultimate tensile strength and total elongation. It was recently reported that improvement in both strength and plasticity of pure zinc can be achieved by alloying with magnesium and by subjecting material to hydrostatic extrusion.[10–12] Those papers focus mainly on

KAROL FRYDRYCH, SAKETH VIRUPAKSHI, and KATARZYNA KOWALCZYK-GAJEWSKA are with the Institute of Fundamental Technological Research (IPPT), Polish Academy of Sciences, Pawinskiego 5B, 02-106 Warsaw, Poland. Contact e-mail: kfryd@ippt.pan.pl ANNA JARZĘBSKA, MAGDALENA BIEDA, ROBERT CHULIST and KRZYSZTOF SZTWIERTNIA are with the Institute of Metallurgy and Materials Science, Polish Academy of Sciences, Reymonta 25, 30-059 Cracow, Poland. MONIKA SKORUPSKA is with the Institute of High Pressure Physics, Polish Academy of Sciences, Sokołowska 29/37 01-142 Warsaw, Poland. NORBERT SCHELL is with the Institute of Materials Research, Helmholtz-Zentrum Geesthacht, Max-Planck-Str. 1, 21502 Geesthacht, Germany.

experimental studies relating microstructure with mechanical properties of pure zinc and low-alloyed zinc with addition of 1 wt pct of Mg.

As already noted, there are not many crystal plasticity studies for Zinc and its alloys (see[13] for an extensive overview), especially as compared with other HCP materials. Moreover, the CP parameters provided in the literature are considerably scattered. Therefore, their identification for these materials is particularly challenging. This task in the case of HCP metals and alloys was usually performed either interactively by researchers (a given person would simulate a given test and visually compare the simulated stress–strain curve or texture with the experimental results until obtaining satisfactory agreement) or using some numerical optimization procedure, as e.g., in Reference 14. In the second case the objective function to be minimized was in most cases the difference between the simulated and experimental stress–strain curves.

In the paper of Solas et al.[15] the N-site visco-plastic self-consistent (VPSC) model was applied to model the texture evolution of high purity zinc subjected to channel die compression. In addition the static recrystallization occurring at post-deformation annealing was modeled using the Monte-Carlo method. Although the study is very interesting and the resulting overall texture evolution seems to be consistent with experiments, the crystal plasticity (CP) modeling framework was not very advanced. In particular, very simple linear hardening law was assumed and single linear hardening modulus was taken for each slip system. The power law exponent used was equal to 5. The values of critical resolved shear stress (CRSS) for the three slip system families considered were chosen approximately without clear justification of the particular values. Twinning was not considered.

The crystal plasticity modelling within both Taylor-type and crystal plasticity finite element method (CPFEM) of zinc-based coating was presented in Reference 16. The dislocation slip on basal, prismatic, pyramidal π_1 and pyramidal π_2 as well as deformation twinning were accounted for. However, it was concluded that the activity of prismatic and pyramidal π_1 slip systems was barely present. The parameters were taken from the relevant literature.

Spherical indentation of zinc single crystal was modelled in Reference 17 in the framework of CPFEM. Dislocation slip on basal, pyramidal and prismatic slip was considered, and basal slip was set as much softer than the other two. Twinning was not considered in the cited paper. The set of parameters was chosen based on[16] so as to obtain both agreement with measured uniaxial anisotropic behavior as well as reasonable hardness values.

In Reference 13, the VPSC model was applied to study the behavior of rolled sheets of Zn-Cu-Ti alloy subjected to uniaxial tension. Covariance matrix adaptation evolution strategy (CMA-ES) was used to obtain the set of material parameters based on the experimental stress–strain curves obtained in tension in 3 directions. Contrary to the previous papers, twinning was also considered. Unfortunately, the authors assume the activity of the tensile twinning $\{10\bar{1}2\}\langle10\bar{1}1\rangle$, while for zinc having the c/a ratio equal to 1.856, the $\{10\bar{1}2\}\langle10\bar{1}1\rangle$ twinning mode should be considered rather as a compressive twinning (i. e. activated when the c axis of the crystal is being compressed) because its c/a ratio is greater than the ideal value of $\sqrt{3}$.[18] Taking this into account, it is hard to say if their modeling approach provides reliable results.

Similarly to op. cit., also in the present paper the evolutionary algorithm (EA) is used in order to identify the CP parameters. Such an approach is chosen mainly due to considerable number of parameters. The in-house python implementation of the EA based on the one described in Reference 19 was already used to optimize the crystal plasticity hardening parameters using both VPSC[3,4,20] and sequential elasto-viscoplastic self-consistent (SEVPSC)[21] models. However, in each case the cost function was built by summing the values of stress in the discrete strain points. In some cases, also the secants to the stress–strain curve were taken into account. Here we propose another approach. In Reference 22, the least squares error between the simulated and experimental orientation distribution function was used as a cost function in the manual optimization of two critical resolved shear stress values. Here we propose to apply similar technique but combine it with the EA. This way it is possible to establish not just two CRSSs but the entire set of crystal plasticity hardening parameters for three slip and one twinning modes.

The paper is structured as follows. In this introductory section, the properties of Zn and its alloys, their modeling using the CP theory as well as optimization of CP parameters have been briefly reviewed. In the following two sections, the experimental methods and the analysis of experimental orientation and texture data from EBSD and synchrotron measurements are included. The fourth section presents the CP framework and the applied evolutionary algorithm with newly developed texture-based fitness function. In the following two sections, the results are collected and discussed. Finally, the paper presents conclusions. In addition, an appendix contains the MTEX function for numerical comparison of two textures.

II. EXPERIMENTAL PROCEDURES

Studied materials were high purity zinc (99.99 pct) and high purity zinc alloyed with 1.5 pct wt. of magnesium (99.99 pct), prepared by gravity casting. Ingots were hot extruded at 250°C with extrusion ratio R = 5.8 and subsequently subjected to multi-pass hydrostatic extrusion (HE) realized in four subsequent passes. As a result, rods with diameter 5 mm and cumulative true strain 3.6 were obtained. Afterwards, samples for microstructural investigation were cut from the received rods so as to observe longitudinal cross-section to extrusion direction. The samples were ground on sand papers with gradation up to 7000 and polished with the use of diamond suspension up to $\frac{1}{4}\mu$m. Finally, the samples were electropolished on Struers LectroPol-5

machine at condition 25 V for 15 seconds in C1 Struers electrolyte. Microstructural experimental data analysis was performed using SEM/ EBSD results. Quanta 3D FEG scanning electron microscope equipped with EDAX TSL OIM system was applied for collecting diffraction patterns. EBSD measurements were analyzed using TSL OIM Analysis 7 software. In order to obtain high-quality statistics, EBSD data were acquired with a different step and map size, depending on the materials' condition. In the case of materials after hot extrusion, a step of 1μm and a size of 1280×1280 μm was selected. A step of 0.2 and 0.1 μm and map size 256×256 μm and 128 x 128 μm were used, for a material after first and consecutive steps of hydrostatic extrusion, respectively. Analysis was performed only for points indexed as α-Zn phase. Second phase of Mg2Zn11 particles[10] is marked by black color on EBSD maps. It was assumed that at least 5 measurement points surrounded by continuous grain boundary with misorientation angle 15 degree is required to fulfill the grain definition. The average grain size (AGS) was determined based on the weighted average grain diameter, where the weight is the grain size (average area fraction). Schmid factor maps were obtained based on the acquired orientation data from TSL OIM analysis for each slip system separately.

The texture of the HE processed materials was measured by high-energy synchrotron radiation ($\lambda = 0.142342$ Å) using the HGZ beamline (P07B) located at PETRA III at DESY in Hamburg. For investigation the 10 mm long specimens were cut from rods. All surfaces were ground with abrasive paper up to 7000 gradation. In order to ensure a good statistics, the specimens were continuously rotated, i.e., individual measuring points were recorded in the angular range ω from -2.5 to 2.5 pct. The obtained Debye–Sherrer rings were transformed into pole figures by StressTexCalculator. For a comparison, EBSD and texture analysis were conducted for pure Zn and Zn-1.5Mg alloy after hot extrusion and after each pass of HE.

III. EXPERIMENTAL RESULTS

In general, hydrostatic extrusion (HE) could be modeled including the entire geometry of the process. However, here we assume that deformation of the
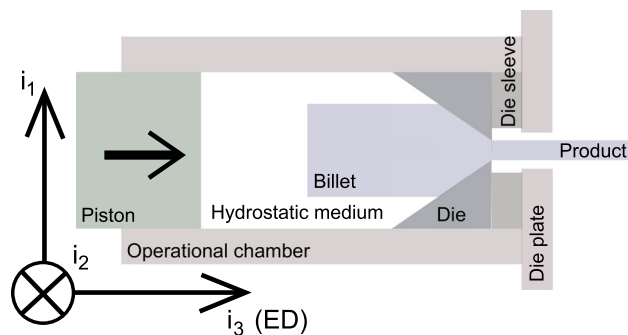
material point near the axis of specimen's symmetry can be approximated using the constant velocity gradient with the following components in the basis $\mathbf{i}_k$ with the direction $\mathbf{i}_3$ along the extrusion direction (ED) (see Figure 1 for the coordinate system):

$$L_{ij} = D_{ij} = \begin{pmatrix} -\frac{1}{2} & 0 & 0 \\ 0 & -\frac{1}{2} & 0 \\ 0 & 0 & 1 \end{pmatrix}. \qquad [1]$$

One HE pass corresponds to 1.0 cumulative strain*, two

---

*The true strain is considered here and calculated as $\epsilon = \ln\left(\frac{A_0}{A_c}\right)$, where A_0 is the initial cross-section of the rod and A_c is the cross-section after a given number of passes.


HE passes to 2.0 strain and four HE passes to 3.6 strain. In the following, the Schmid factor (SF) maps calculated based on the experimental results for pure Zn will be shown for the initial state and after 1 and 4 HE passes. The orientation maps are also presented. In the case of Zn-1.5Mg alloy only the SF maps before HE and after first and second passes will be shown. The dominant mechanism of microstructure evolution after more than two HE passes was significantly changed for this alloy and investigation of this particular phenomenon is outside the scope of the paper.

Figures 2 and 3 present EBSD data analysis using TSL OIM ANALYSIS 7 software. SF maps were obtained for the longitudinal cross sections (LCS) to the extrusion direction using orientation data and the stress deviator of the same form as the strain rate tensor given by Eq. [1]. For each map average grain size was calculated. In the case of pure zinc, the largest reduction of the grain size was observed after the first pass and microstructure with equiaxed grains was obtained. After next passes only slight difference was observed in the size and shape of grains. The initial microstructure of Zn-1.5Mg alloy is considerably different, namely, two phases are present: α-Zn and eutectic composed of α-Zn and Mg2Zn11 intermetallic phase. The grains are elongated in the extrusion direction. The α-Zn grains are larger than eutectic grains but they are much smaller than the grains present in pure Zinc. Further reduction of grain size can be seen in the second HE pass. The small equiaxed grains of α-Zn are separated by eutectic bands, which are also getting narrower after additional passes of extrusion.

The partition fraction of Schmid factor value exceeding 0.4 for each slip system is presented on the graphs in Figures 2(b) and 3(b) for each pass for pure Zn and Zn-1.5Mg alloy, respectively. The correlation between AGS, elongation to fracture ϵ_f and Schmid factor for different slip systems is also presented. In the case of hydrostatic extrusion the calculated Schmid factor on slip systems other than basal is high. This can lead to their activation provided that also the critical value of the resolved shear stress (RSS) at a given temperature for those systems is sufficiently low. In the case of pure Zn, the compressive twinning presents significant

Fig. 1—HE scheme (according to Ref. 23) along with the coordinate system.
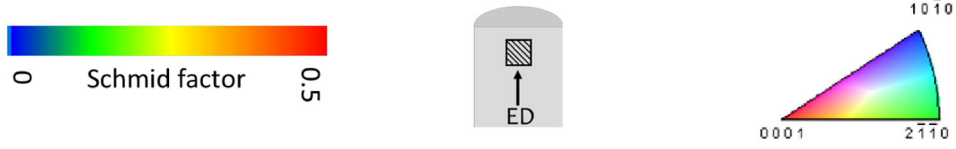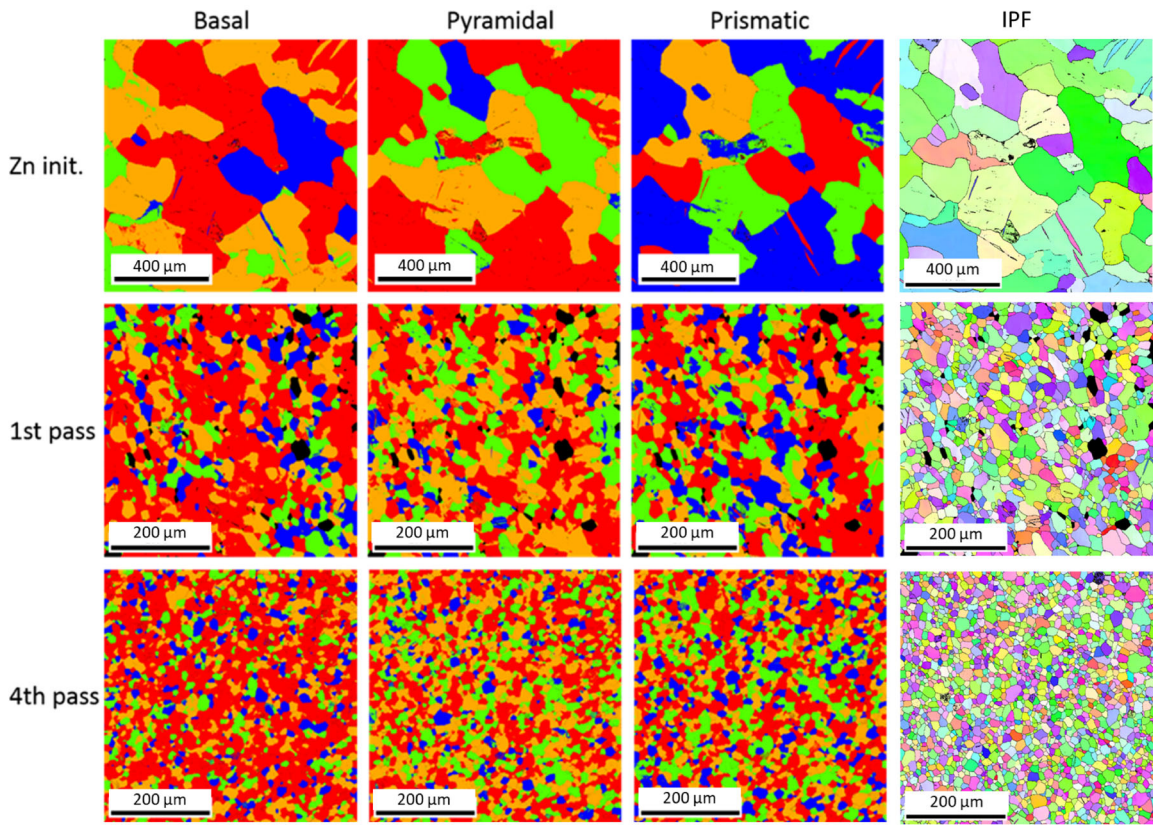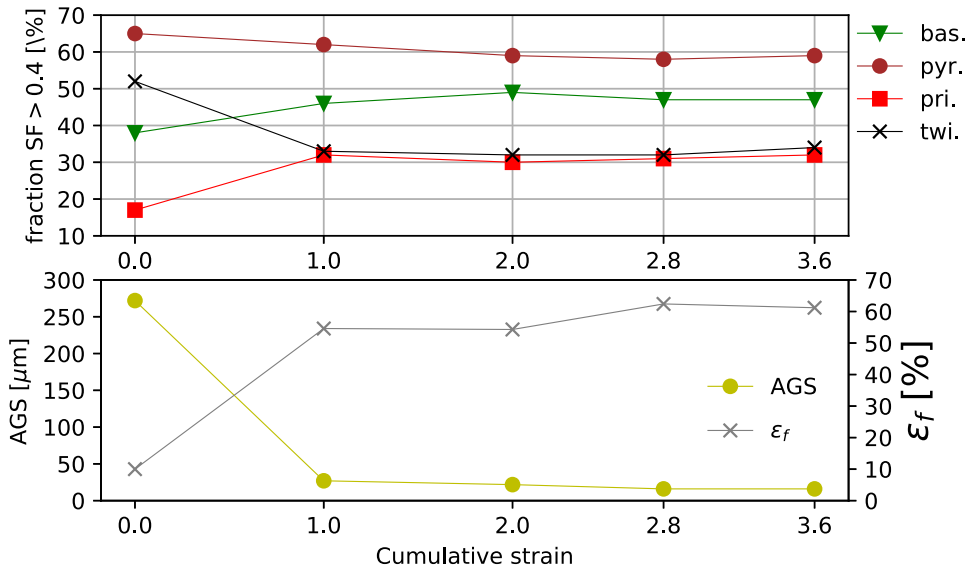
Fig. 2—(a) EBSD maps of the Schmid factor for the basal, pyramidal $<c+a>$ $\{11\bar{2}2\}\langle\bar{1}\bar{1}23\rangle$ and prismatic slip systems and crystallographic orientation[10] for different passes for pure Zn. Note that the scale changes for different passes. (b) Partition fraction of map points for which Schmid factor > 0.4 with corresponding evolution of average grain size (AGS) and elongation to fracture ϵ_f.

Schmid factor in the first HE pass but it decreases in subsequent passes. The pyramidal $<c+a>$ $\{11\bar{2}2\}\langle\bar{1}\bar{1}23\rangle$ and prismatic slip systems can be characterized as possessing significantly high values of the Schmid factor, especially in the case of Zn-1.5Mg alloy. However, according to the literature (cf.[13,15–17] and references cited therein), the critical resolved shear stress for basal slip for Zn and its alloys is the lowest. Taking into account both the value of SF and the CRSS, it seems that in the case of pure zinc the basal slip should be the most active system after second pass.

Figure 4 shows the pole figures obtained from the texture measured for the initial texture (after hot extrusion but before HE) of (a) pure Zn and (b) Zn-1.5Mg alloy. These pole figures (and all the other pole figures presented next) were plotted using the MTEX software.[24] One can see that the initial texture is close to the ring texture with the basal planes being parallel to the extrusion direction. However, the circular symmetry is not observed, as some localization of the basal planes can be seen. The prismatic planes show even more localization. Judging from our previous results for α-Ti[1] it can be surmised that the prismatic slip could be the primary deformation mechanism in the course of the initial hot extrusion. Verfication of this observation is however outside the scope of the present paper.

Figures 5 and 6 show the pole figures obtained from the textures after HE measured for pure zinc and the Zn-1.5Mg alloy, respectively. One can see that the texture of pure Zn after the 1st HE pass (Figure 5(a)) can be characterized by the basal plane normals being inclined about 70 degree to the rod axis. Contrary to the initial texture, the poles are distributed quite uniformly around ED. In addition, there is a local (0001) maximum corresponding to grains having the basal plane normal nearly aligned with ED. It seems to result from the activity of twinning and this view will be discussed later. The texture after second (Figure 5(b)) and fourth (Figure 5(c)) HE passes is similar but lacks the central maximum. The origin of its disappearance is not obvious and shall be discussed later. The texture for Zn-1.5Mg (Figure 6) is similar, but the two main fibres are present in different proportions. Clearly, after the first HE pass (Figure 6(a)) the central (0001) maximum is more intense than the 70 degree inclined ring. This changes after second pass where the ring fibre is more intense. However, the central component does not disappear as it was the case for pure Zn.

IV. MODEL

A. *The Mean Field Crystal Plasticity Model*

The crystal plasticity model and implementation is exactly the same as in Reference 1. It will be however described here for the sake of completeness. The multiplicative decomposition of the deformation gradient into elastic and plastic parts results in the additive decomposition of the velocity gradient $\mathbf{l}$:

$$\mathbf{l} = \mathbf{l}^{\mathrm{e}} + \mathbf{l}^{\mathrm{p}}, \qquad [2]$$

where the indices e and p refer to elastic and plastic parts. Since the elastic stretches are disregarded, the elastic part of the velocity gradient is equal to the lattice spin:

$$\mathbf{l}^{\mathrm{e}} = \boldsymbol{\omega}^{\mathrm{e}}. \qquad [3]$$

As usual in crystal plasticity, twinning is considered as a pseudo-slip, cf.[25–27]:

$$\dot{\gamma}^l = \gamma^{TW,l}\dot{f}^l, \qquad [4]$$

where $\dot{f}^l$ is the rate of the volume fraction increase of the l-th twinning system and $\gamma^{TW,l}$ is its characteristic twin shear. Moreover, the characteristic twin shear of the $\{10\bar{1}2\}\langle10\bar{1}\bar{1}\rangle$ compressive twinning can be calculated as[18]:

$$\gamma^{TW} = \frac{(c/a)^2 - 3}{\sqrt{3}(c/a)}, \qquad [5]$$

which yields the value of 0.138 for zinc where the c/a ratio is equal to 1.856.

The plastic part of the velocity gradient is a sum of shears on slip and twinning systems:

$$\mathbf{l}^{\mathrm{p}} = \sum_{k=1}^{2M} \dot{\gamma}^k \mathbf{m}^k \otimes \mathbf{n}^k + \sum_{l=1}^{N} \dot{\gamma}^l \mathbf{m}^l \otimes \mathbf{n}^l, \qquad [6]$$

where $\dot{\gamma}^{k(l)} \geq 0$ is the rate of shearing on the $k(l)$-th slip or twinning system, M and N are the number of slip and twinning systems (note that in the sum $2M$ and N is used to account for the unidirectionality of twinning).

The rate of shearing on a given system (slip or twinning) r is obtained as:

$$\dot{\gamma}^r = \dot{\gamma}_0 \left(\frac{\tau^r}{\tau_{\mathrm{c}}^r}\right)^n, \qquad [7]$$

where $\dot{\gamma}_0$ is the reference shear rate equal to 0.001. τ^r is the non-negative resolved shear stress calculated using:

$$\tau^r = <\mathbf{m}^r \cdot \boldsymbol{\sigma} \cdot \mathbf{n}^r>, \text{ where} < \cdot > \equiv \frac{1}{2}((\cdot) + |\cdot|) \quad [8]$$

$\boldsymbol{\sigma}$ is the Cauchy stress, $\mathbf{m}^r$ is the system's r direction vector and $\mathbf{n}^r$ is its' plane normal vector.

The viscoplastic self-consistent (VPSC) code[28,29] in the VPSC-7 version[30] is applied. The code was enriched by implementation of the probabilistic twin volume consistent (PTVC) reorientation scheme[31] and modified hardening laws.[32] The aim of the PTVC scheme is to ensure the consistency between the volume fraction of twins $\dot{f}^l$ calculated using the Eq. [4] and the volume fraction of the reoriented grains. This is performed in a statistical fashion.

The hardening model governs the evolution of the critical resolved shear stresses (CRSSs) τ_{c}^r due to self and mutual slip-twin interactions. The hardening law for slip ($r \leq M$) and twinning ($r > 2M$) are defined as follows:
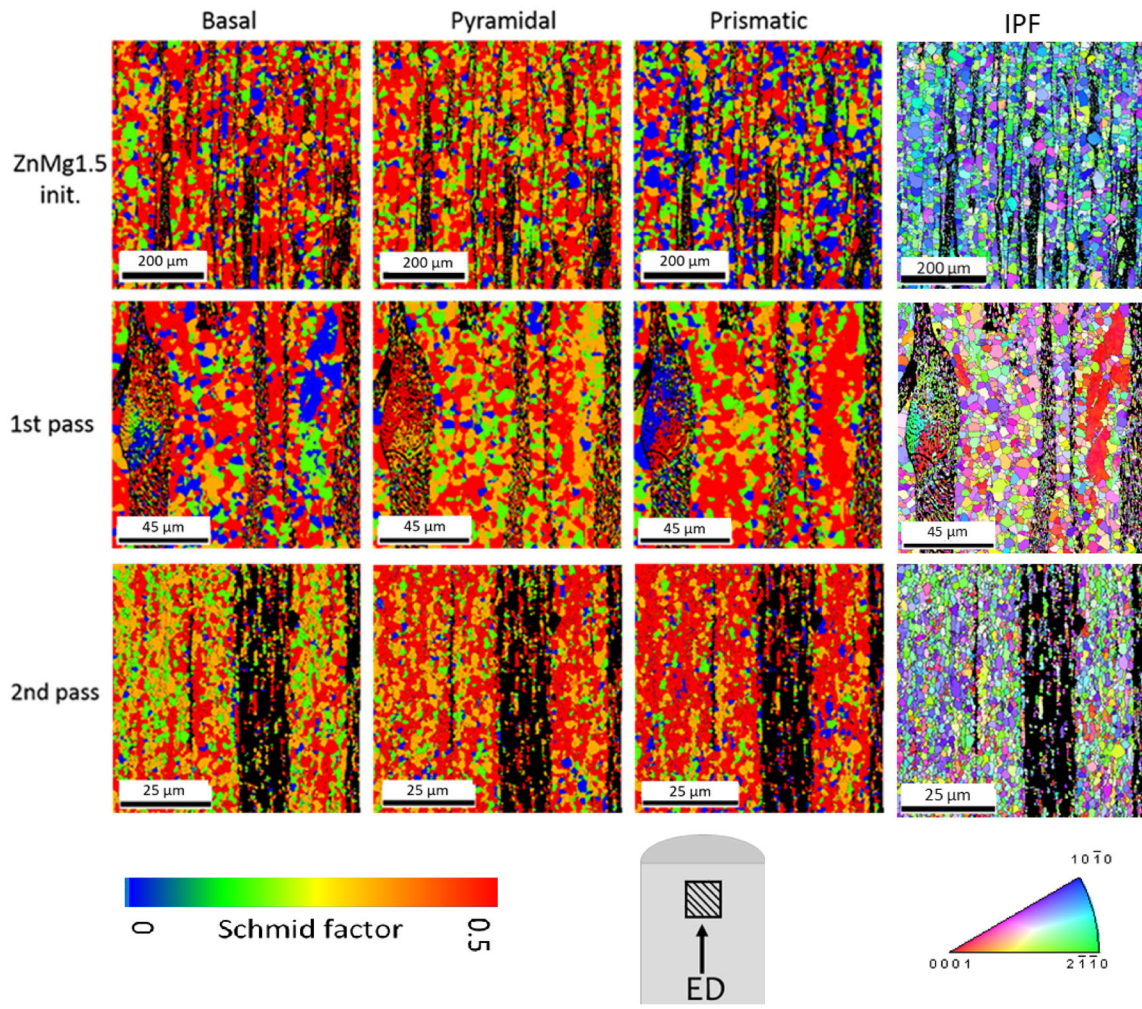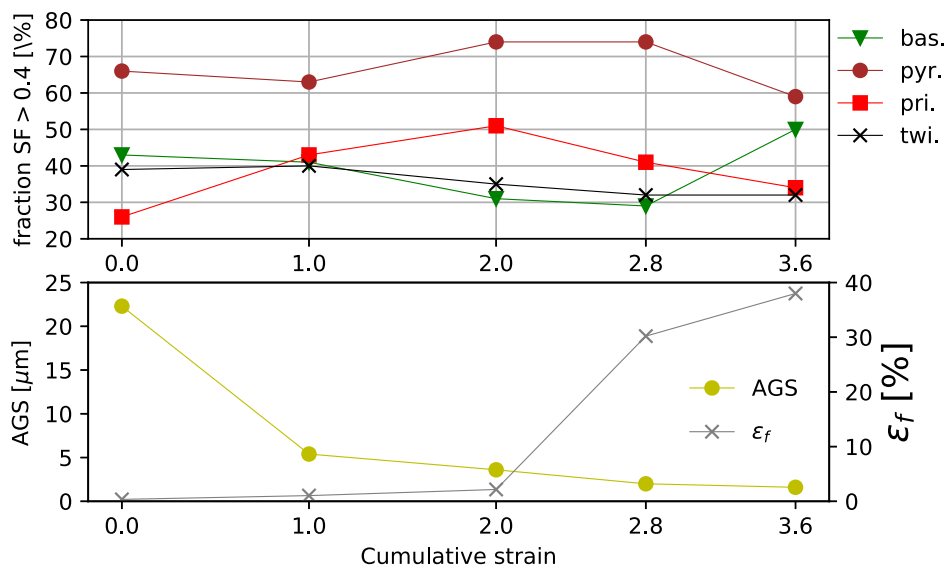
Fig. 3—(a) EBSD maps of the Schmid factor for the basal, pyramidal $<c+a> \{11\bar{2}2\}\langle\bar{1}\bar{1}23\rangle$ and prismatic slip systems and crystallogrphic orientation for different passes for Zn-1.5Mg alloy. Note that the scale changes for different passes. (b) Partition fraction of map points for which Schmid factor > 0.4 with corresponding evolution of average grain size (AGS) and elongation to fracture ϵ_f.
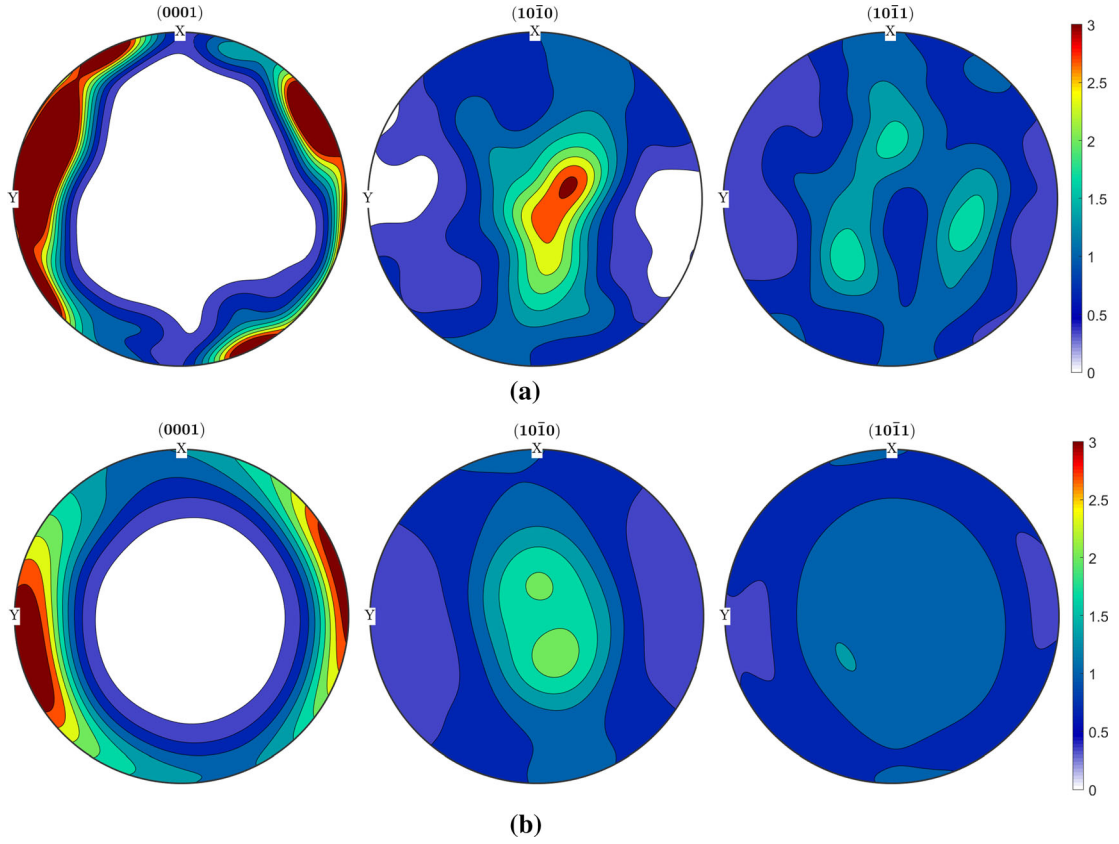
Fig. 4—The initially measured texture of (*a*) pure zinc and (*b*) Zn-1.5Mg alloy. ED is normal to the plane of the image. The pole figures were plotted using the MTEX[24] software.

$$\dot{\tau}_{\mathrm{c}}^{r} = \dot{\tau}_{\mathrm{c}}^{r+M} = H_{(\mathrm{ss})}^{r} \sum_{q=1}^{M} h_{rq}^{(\mathrm{ss})} \dot{\bar{\gamma}}^{q} + H_{(\mathrm{st})}^{r} \sum_{q=2M+1}^{2M+N} h_{rq}^{(\mathrm{st})} \dot{\gamma}^{q}, \quad [9]$$

where

$$\dot{\bar{\gamma}}^{q} = \dot{\gamma}^{q} + \dot{\gamma}^{q+M}$$

and

$$\dot{\tau}_{\mathrm{c}}^{r} = H_{(\mathrm{ts})}^{r} \sum_{q=1}^{M} h_{rq}^{(\mathrm{ts})} \dot{\bar{\gamma}}^{q} + H_{(\mathrm{tt})}^{r} \sum_{q=2M+1}^{2M+N} h_{rq}^{(\mathrm{tt})} \dot{\gamma}^{q}, \quad [10]$$

respectively. The self-hardening moduli $H_{(\alpha\beta)}^{r}$ present in Eqs. [9] and [10] are defined in the following way for hardening of slip ($\alpha = s$) or twin ($\alpha = t$) systems due to activity of slip (s):

$$H_{(\alpha\mathrm{s})}^{r} = h_{0}^{\alpha\mathrm{s}} \left(1 - \frac{\tau^{r}c}{\tau_{\mathrm{sat}}^{r}} \right)^{\beta} \quad [11]$$

and as follows due to actvity of twinning (t):

$$H_{(\alpha\mathrm{t})}^{r} = \frac{h_{0}^{\alpha\mathrm{t}}}{\tau_{\mathrm{c}}^{r}} \left(\frac{f^{\mathrm{TW}}}{f_{\mathrm{sat}}^{\alpha\mathrm{t}} - f^{\mathrm{TW}}} \right). \quad [12]$$

The latent hardening on coplanar and non-coplanar systems is distinguished:

$$h_{rq}^{(\alpha\beta)} = q^{(\alpha\beta)} + (1 - q^{(\alpha\beta)}) |\mathbf{n}^{r} \cdot \mathbf{n}^{q}|. \quad [13]$$

As can be deduced from the equations, the evolution of CRSSs due to twin has an S-shape, while the evolution of CRSSs due to slip is exponential. It should be stressed that the present formulation does not take into account the influence of temperature variation during the process on the material behavior. Dynamic recrystallization phenomenon is also beyond the scope of model applicability. Nevertheless the model is able to predict activity of subsequent slip and twin systems as well as texture evolution induced by the applied plastic deformation process.

B. *Evolutionary Algorithm*

The comprehensive review of evolutionary algorithms can be found *e.g.*, in Reference 33 or 34. In general, the genotype and phenotype can be distinguished in EA. The genotype in this case would be a long list of zeroes and ones which should be then translated into the phenotype, that is the hardening parameters. The present implementation is however based on the paper of Skippon, Mareau and Diamond[19], where the binary genotype is omitted. Instead, all genetical operations are directly applied to the phenotype. Although this approach is less mathematically sound as there are no theorems that could prove its efficiency or supply the
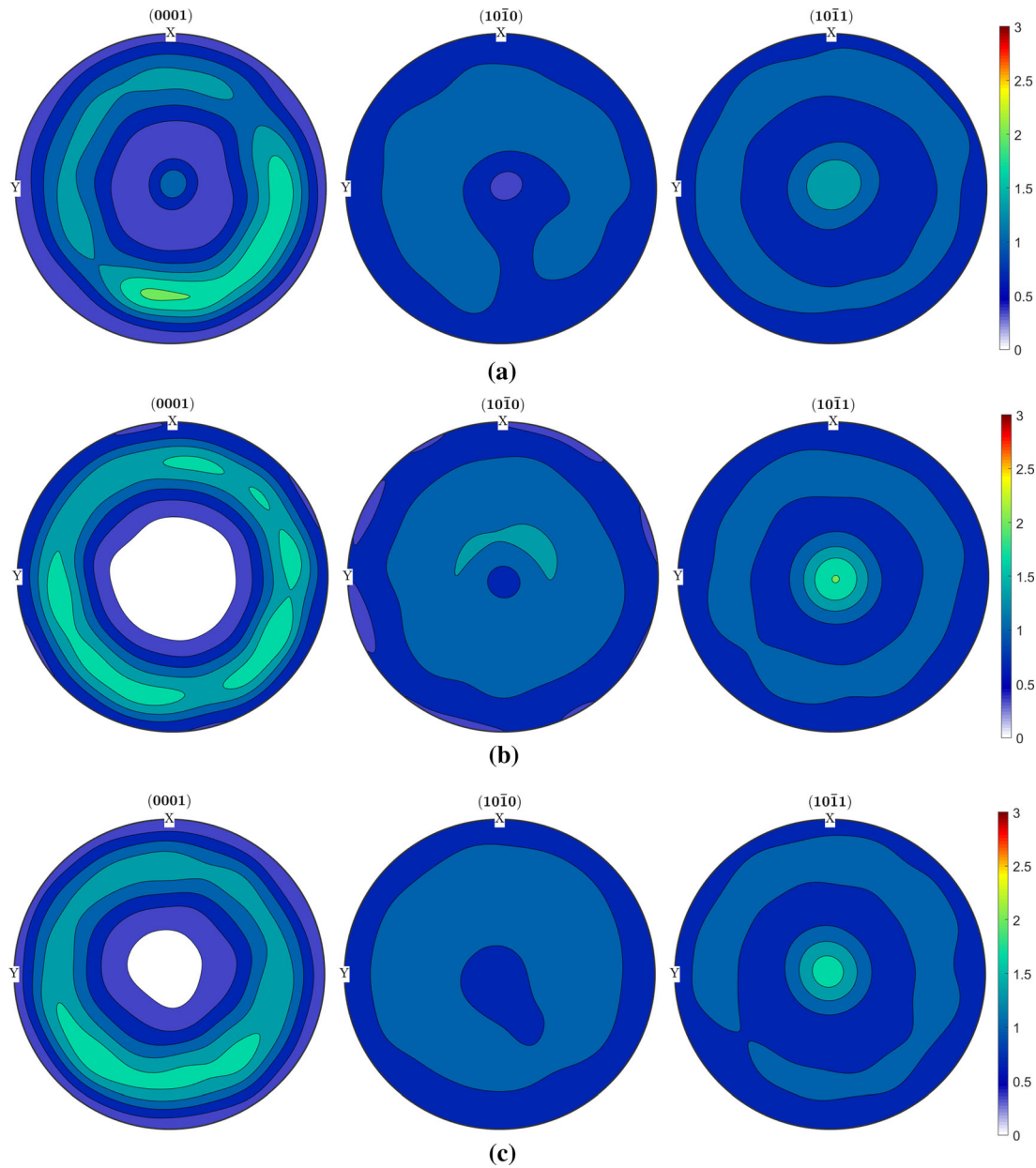
Fig. 5—The texture of the pure Zn measured after (*a*) 1.0, (*b*) 2.0 and (*c*) 3.6 strain. ED is normal to the plane of the image. The pole figures were plotted using the MTEX[24] software.

bounds of the parameters of the algorithm itself, it is relatively simple in implementation and provides satisfactory results.

The evolutionary algorithm code has been written in the Python programming language. Similar EA implementation was already described in References 3, 20, and 21 and the only crucial difference is the fitness function used here. For convenience of the reader, the EA is again described in the following. First, the minimum and maximum values of the parameters have to be specified. The ranges of parameters for both pure zinc and Zn-1.5Mg alloy are given in Table I. The program randomly generates 7 hardening parameters for every slip mode and 5 hardening parameters for the compression twinning. In addition, four latent hardening parameters are randomly generated for each mode. This procedure is performed for each of the N_{ind} individuals. Then, the program performs the VPSC simulations by calling the external VPSC executables. This step is done in parallel which greatly increases the computational efficiency. Then, the evaluation of the fitting of each individual is conducted. Contrary to[3,20,21], the evaluation is done by comparing the simulated texture with the experimental one. This is also done in parallel, this time using the Matlab toolbox MTEX.[24,35] Using the software, the ODFs of both textures are first generated based on the discrete orientation sets. Then, the texture index of the difference between the ODFs is calculated. This number is dived by the texture index of the experimental ODF thus yielding the normalized texture index of the
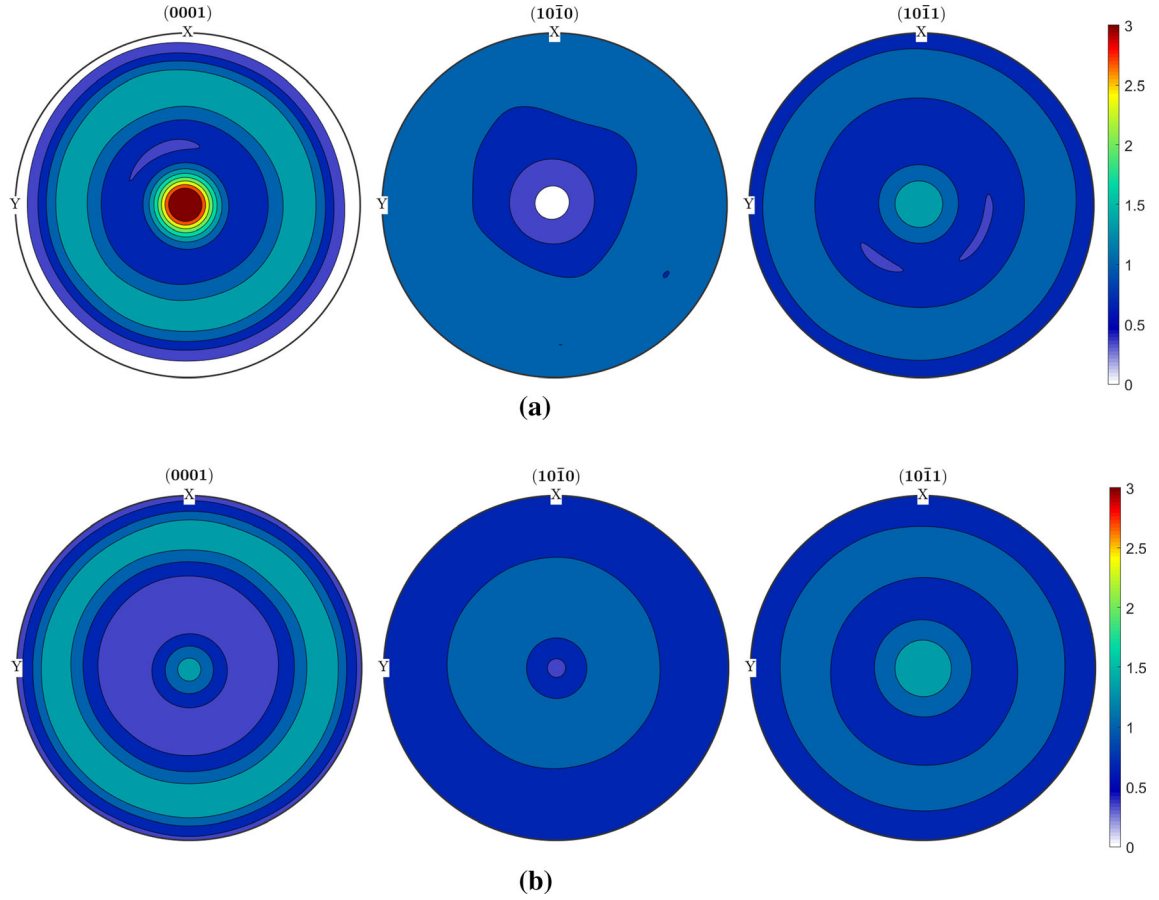
Fig. 6—The texture of the Zn-1.5Mg alloy measured after (*a*) 1.0 and (*b*) 2.0 strain. The pole figures were plotted using the MTEX[24] software. ED is normal to the plane of the image.

Table I. The Ranges of the VPSC Model Parameters Specified for the Optimization for the Both Materials

System	Interaction	τ_{c0} [MPa]	h_0 [MPa]	τ_{sat}/f_{sat} [MPa]/–	μ –	β –	q
Basal	slip-slip	1.0	1.0-50.0	1.0-10.0	1.0-5.0	1.0-10.0	0.5-2.0
	slip-twin	—	0.0-1.0	0.1-2.0		—	
Pyram.	slip-slip	2.0-15.0	1.0-100.0	2.0-30.0	1.0-10.0	1.0-20.0	0.5-2.0
	slip-twin	—	0.0-1.0	0.1-2.0		—	
Prism.	slip-slip	4.0-30.0	1-200.0	4.0-60.0	1.0-20.0	1.0-40.0	0.5-2.0
	slip-twin	—	0.0-1.0	0.1-2.0		—	
C1	twin-slip	—	1.0-10.0	—	0.5-2.0	—	0.5-2.0
	twin-twin	1.0-10.0	0.0-2.0	0.3-1.0		—	

Abbreviations: Pyram. – Pyramidal $\pi_2 \langle c+a \rangle$, Prism. – Prismatic. $n = 20$, $\dot{\gamma}_0 = 0.001 \frac{1}{s}$ is assumed.

ODF difference (NTID). The whole function for comparing the textures is presented in Appendix. Sum of NTIDs at specified strain points (*e.g.*, for pure zinc the NTID was calculated after 1.0, 2.0 and 3.6 strain) serves as the cost value. After evaluation of individuals, the set containing N_{hri} highest ranked individuals (HRI) is selected by choosing individuals with lowest values of the cost function.

Contrary to the parameters of the individuals belonging to the first generation, the parameters of the individuals belonging to the second generation (and every other out of N_{gen} generations) are selected using crossover and mutation. The crossover is performed as follows. For each individual, two parent individuals are randomly selected from the set of HRI. Then, the number α from the range 0 to 1 is generated. Each hardening parameter of the child is then calculated as follows:

$$HP_{child,i} = \alpha * HP_{parent1,i} + (1-\alpha) * HP_{parent2,i}, \quad [14]$$

where obviously $HP_{child,i}$, $HP_{parent1,i}$ and $HP_{parent2,i}$ is the *i*-th hardening parameter of the child and 1st and 2nd

parent, respectively. We should note here that the simple EA does not account for the individual's sex, that's why *parent*1 and *parent*2 notions are used, rather than father and mother which would be the case in the reproduction of mammals or birds. The individual can be however related to some hermaphrodite species such as certain snails.

The important part of the EA is also mutation. After the crossover is finished, each hardening parameter can be again randomly generated from the initially supplied parameter ranges. This is done every time the randomly generated number from the interval 0 to 1 is lower than the specified mutation probability P_{mut}. Accounting for the mutations enables to overcome local minima and diminish the possibly negative effect of badly chosen initial set. Choosing the value of P_{mut} is a delicate issue. Too low value makes it more probable to converge to some local minimum, while too high value increases the probability of reaching the maximum specified number of generations N_{gen} before converging to the solution.

In simulations, we assume that both pure Zinc and its alloy with magnesium deform plastically by dislocation glide on 3 slip systems, namely basal $\{0001\}\langle 2\bar{1}\bar{1}0\rangle$, pyramidal $<c+a>$ $\{11\bar{2}2\}\langle\bar{1}\bar{1}23\rangle$ and prismatic $\{10\bar{1}0\}\langle\bar{1}2\bar{1}0\rangle$. Plastic deformation is also partially accommodated by $\{10\bar{1}2\}\langle10\bar{1}\bar{1}\rangle$ compressive twinning. As a result, 43 hardening parameters (including 16 latent hardening parameters) are employed in the single crystal model. This is the main reason why applying the EA optimization is a good choice here. It should be noted that only relative values of the hardening parameters are established here ($\tau_0 = 1.0$ MPa is prescribed for the basal slip family). However, using the yield stress obtained for the raw material, the exact values of the hardening coefficient could be simply obtained by scaling the hardening parameters using just one number so that the simulated and measured yield stress match.

The following parameters of the algorithm were applied: number of individuals $N_{ind} = 100$, number of highest ranked individuals in each generation $N_{hri} = 20$, maximal number of generations $N_{gen} = 200$ and probability of mutation $P_{mut} = 0.1$. In addition the algorithm would stop if the mean standard deviation of the fitness values of the set of HRIs was lower than 0.002. The reason why we account for the HRIs and not the entire population itself is the occurrence of relatively frequent mutations and the fact that only the HRIs are selected to reproduce in subsequent populations. Therefore, even if there are individuals that have significantly different (but higher than those of the HRIs) values of the fitness function they will not lead to any improvement of the parameter set. The VPSC's input texture was obtained by discretization of the measured texture into 1000 orientations using the ATEX software.[36] The discretized initial texture is presented in Figure 7. Comparing this texture to the original one presented in Figure 4 one can see that only moderate differences are present.

V. RESULTS

A. *Pure Zinc*

In the case of pure Zinc, the EA achieved almost uniform population after 114 generations. The resulting set of parameters is shown in Table II. The resulting texture is presented in Figure 8. It can be compared with the experimental texture (Figure 5). The texture after 1.0 strain (one HE pass) is fitted reasonably well. The most important features of the texture after 2.0 (two HE passes) and 3.6 (four HE passes) are also fitted correctly. Especially, the strong ring near the periphery of the (0001) pole figure and strong maximum in the centre of the (10$\bar{1}$1) pole figure together with a weaker ring around it are present. Unfortunately, the maximum in the center of the (0001) pole figure is present not only after 1.0 (as is the case in the measured texture) but also after 2.0 and 3.6. The appearance of this maximum is the result of twinning. Its disappearing after further passes observed in experiments could be the result of either detwinning or destruction of twins be means of some recrystallization processes. However, detwinning does not seem to be a viable explanation, because the process does not involve strain path changes. Thus, more probable explanation seems to be the recrystallization not accounted for in the present modeling framework. This shall be further discussed in the *Discussion* section.

Figure 9 presents the relative activities of the slip and twinning systems during the simulation of HE applied to pure zinc. It can be seen that initially only the basal slip and twinning are activated. The twin volume fraction (blue line) quickly achieves around 45 pct and saturates. Then the pyramidal and prismatic systems are activated. However, their CRSSs quickly increase and their activity drops. Finally, some steady state seems to be achieved, when the ratios of the activities of basal, pyramidal and prismatic slip are more or less constant.

In general, these results are consistent with the SF results presented in Figure 2. As the SFs for the basal and pyramidal slip systems in the initial material are high, their activities are also considerable. Of course, basal slip shows more activity due to its lower CRSS. Also the high initial activity of twinning is consistent with its high SF. On the contrary, prismatic slip is activated to a limited extent, due to its low SF in most of the grains. In subsequent passes, the SFs for the basal and pyramidal slip are nearly constant and this is also reflected in their nearly steady-state activities. Due to the nature of twinning, it cannot be activated any more after the TVF reaches saturation. Also, its SF in subsequent passes decreases. In addition, it is often argued that twinning is difficult to activate in small grains and there is a considerable grain refinement in subsequent HE passes. The SF for the prismatic slip system in the second and following passes is higher than in the first one, but it is still lower than in the case of basal and pyramidal systems. Nevertheless, very high CRSS and strain-hardening moduli predicted by EA for this system lead to its almost negligible activity.
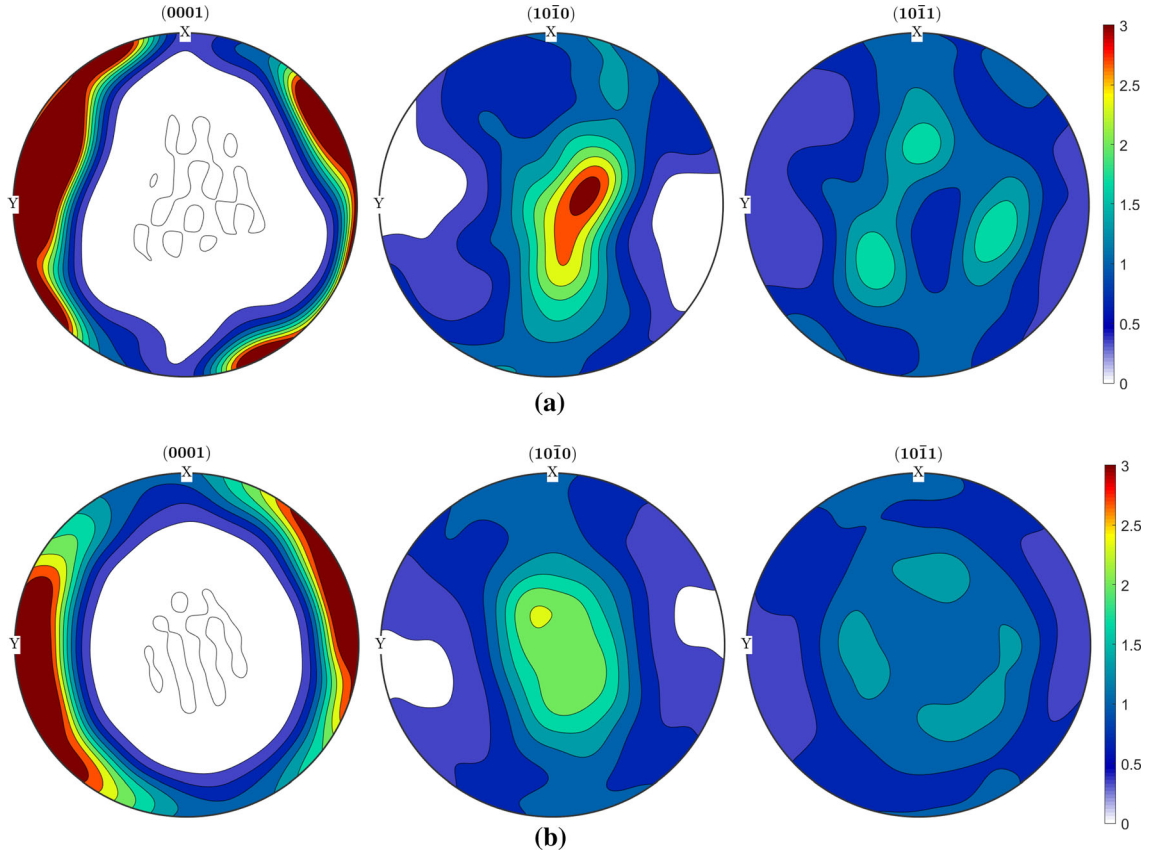
Fig. 7—The measured initial texture of (*a*) pure zinc and (*b*) Zn-1.5Mg alloy discretized into 1000 orientations. ED is normal to the plane of the image. The pole figures were plotted using the MTEX[24] software.

Table II. The Hardening Parameters of the VPSC Model Established Using the EA Algorithm for Pure Zinc

System	Interaction	τ_{c0} [MPa]	h_0 [MPa]	τ_{sat}/f_{sat} [MPa]/–	μ —	β —		q —	
Basal	slip-slip	1.0	32.12	8.06	3.95	2.47	1.28	1.18	1.19
	slip-twin	—	0.53	0.76	—	—		0.96	
Pyram.	slip-slip	7.15	56.6	11.86	3.42	15.97	1.13	1.27	1.35
	slip-twin	—	0.43	0.78	—	—		1.17	
Prism.	slip-slip	10.49	105.59	20.34	8.26	27.95	1.22	1.40	1.21
	slip-twin	—	0.43	0.38	—	—		1.20	
C1	twin-slip	—	4.39	—	1.09	—	1.17	1.24	1.01
	twin-twin	6.99	0.76	0.67	—	—		1.02	

$n = 20$, $\dot{\gamma}_0 = 0.001 \frac{1}{s}$ is assumed.

B. *Zn-1.5Mg Alloy*

In the case of the alloy, only textures after 1.0 (one HE pass) and 2.0 (two HE passes) were used for the fitting. 50 generations were sufficient for the code to obtain almost uniform set of HRI. The obtained set of parameters is presented in Table III. It should be noted that only the α-Zn phase is considered. This approach is fully justified as also in the texture measured experimentally only this phase is taken into account. The resulting texture is presented in Figure 10. It can be seen (by comparing with Figure 6) that the overall texture is correctly fitted although some features clearly differ. In

general, the texture after 1.0 is fitted better than the one after 2.0. Especially, the VPSC model again failed to predict the diminishing of the maximum in the centre of the (0001) pole figure.

The slip system activities are shown in Figure 11. These results are similar to the pure zinc, however, the saturated TVF is somewhat smaller and the activities of pyramidal and prismatic slip systems relative to the basal slip are larger. In addition, in the final stage of the process no steady state is observed. On the contrary, the basal slip activity drops down and the activity of the prismatic slip increases. Comparing with the results for
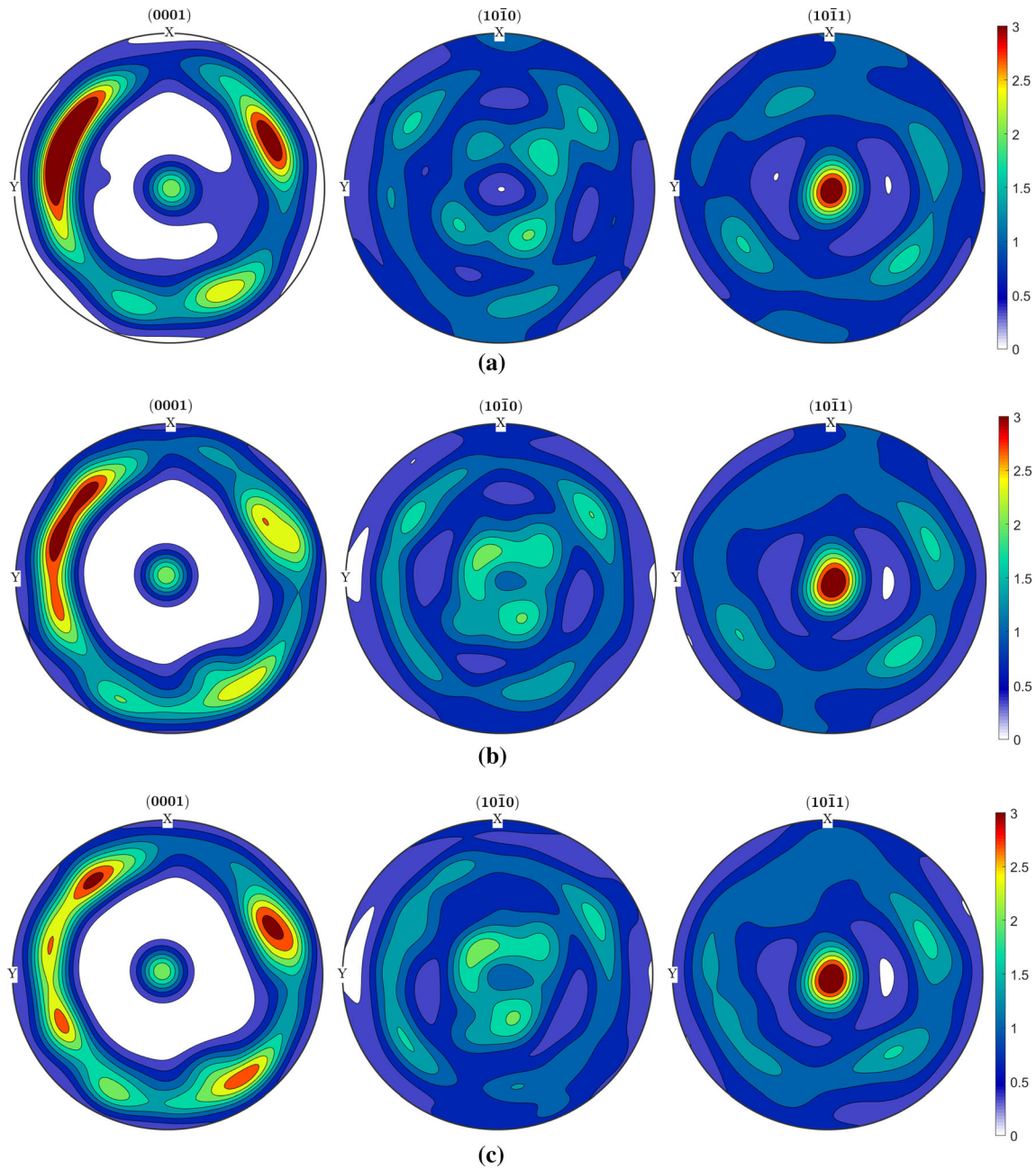
Fig. 8—The simulated texture of pure Zn after (a) 1.0, (b) 2.0 and (c) 3.6 strain. The pole figures were plotted using the MTEX[24] software. ED is normal to the plane of the image.
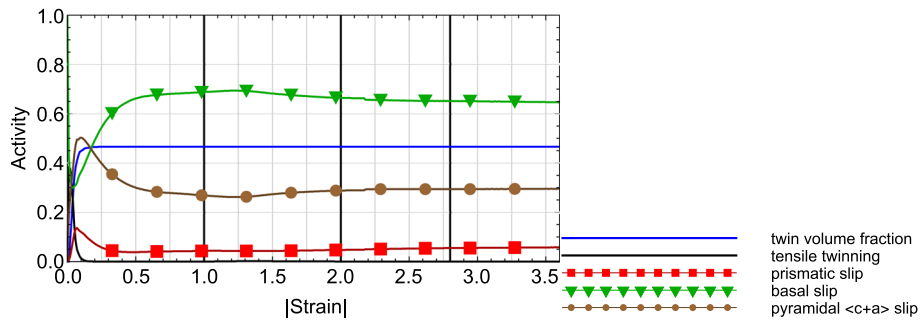

Fig. 9—The simulated slip and twinning systems activities in the simulation of HE applied to pure Zn.

Table III. The Hardening Parameters of the VPSC Model Established Using the EA Algorithm for Zn-1.5Mg Alloy

System	Interaction	τ_{c0} [MPa]	h_0 [MPa]	τ_{sat}/f_{sat} [MPa]/–	μ	β		q	
Basal	slip-slip	1.0	21.73	8.62	4.71	4.07	1.31	1.35	1.22
	slip-twin	—	0.27	0.56	—	—		1.26	
Pyram.	slip-slip	7.39	41.25	15.12	7.90	13.03	0.95	1.11	1.40
	slip-twin	—	0.66	1.13	—	—		1.41	
Prism.	slip-slip	9.76	131.58	22.61	1.87	20.52	1.12	1.43	1.31
	slip-twin	—	0.63	0.37	—	—		1.29	
C1	twin-slip	—	3.25	—	1.45	—	1.02	1.26	0.97
	twin-twin	8.27	1.01	0.75	—	—		1.21	

$n = 20$, $\dot{\gamma}_0 = 0.001 \frac{1}{s}$ is assumed.

pure Zn and the SF results shown in Figure 3 it can be stated that the resulting differences are mainly due to different crystallographic orientations. As the SFs for the pyramidal and prismatic slip systems are higher than in the case of pure Zn, also their predicted activities are higher. Especially, while in pure Zn, the SFs did not change much in subsequent HE passes, the SFs of the alloy after two HE passes are considerably different from those after the first pass. This seems to be the reason for the lack of steady-state in this case. Clearly, the decrease of the basal slip activity in the second pass corresponds to its decreasing SF. This decrease is assisted by the increase of the activity of the prismatic slip—the increase of its Schmid factor can be clearly observed in Figure 3.

VI. DISCUSSION

The first question to be discussed is the origin of the ⟨0001⟩‖ED fibre. To show that its appearance results from the reorientation related to twinning, the simulation with the same parameters but without considering twinning was carried out for Zn-1.5Mg alloy. The
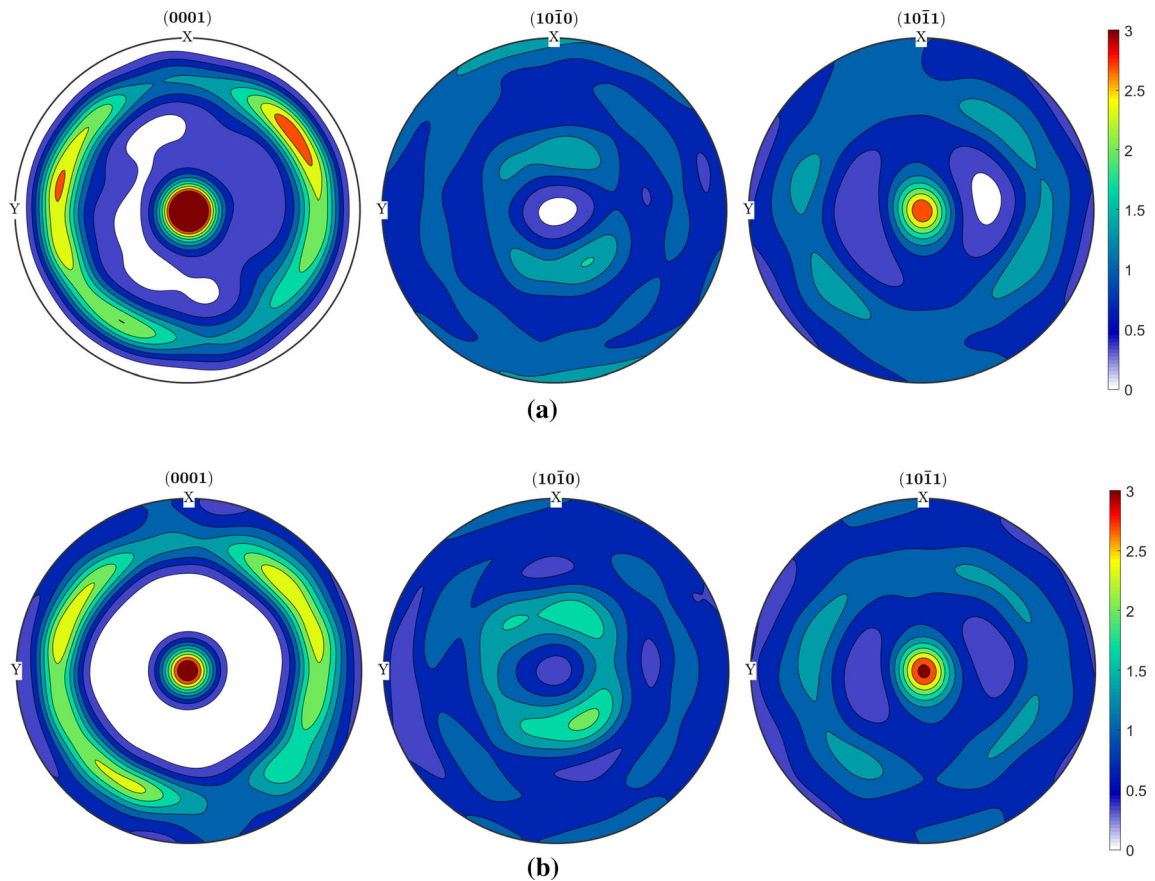

Fig. 10—The simulated texture of Zn-1.5Mg alloy after (a) 1.0 and (b) 2.0 strain. The pole figures were plotted using the MTEX[24] software. ED is normal to the plane of the image.
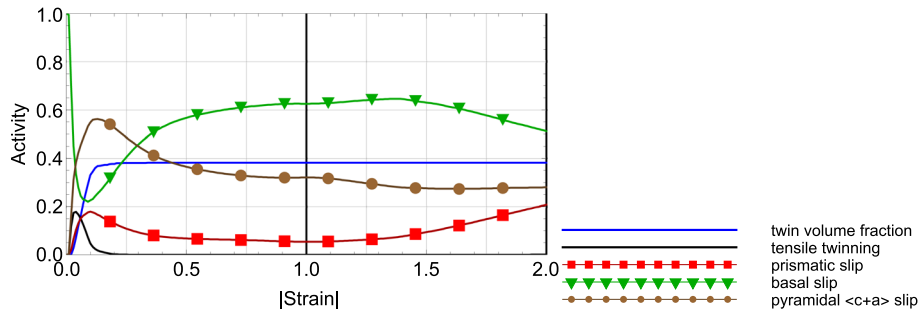
Fig. 11—The simulated slip and twinning systems activities in the simulation of HE applied to Zn-1.5Mg alloy.

resulting texture after one HE pass is presented in Figure 12. It can be clearly seen that in such a case, this component is not present. Thus, its twinning-related origin is confirmed.

The main disagreement of the presented modeling results as compared to the experimental results is too strong $\langle 0001 \rangle \| ED$ fibre after 2nd and subsequent passes. The probable reason for its disappearance observed in experiments shall be discussed in the following. In the paper of Solas et al.[15] the static recrystallization of high purity zinc was studied both experimentally and using the Monte Carlo approach. The authors concluded that the nucleation occurs in highly deformed grains and then it proceeds by growth into the less deformed grains. The grains with their 'c' axis nearly perpendicular to the channel die compression axis are hard to deform by the easy basal slip. As a result they do not deform much, their stored energy is relatively low and they are consumed by other growing crystallites. Here, the central (0001) maximum corresponds to grains whose 'c' axis is nearly aligned with ED. The Schmid factor of an ideal $\langle 0001 \rangle \| ED$ orientation for basal slip with respect to the stretching force along ED is:

$$m = \cos 0 \deg \cdot \cos 90 \deg = 0. \qquad [15]$$

Therefore, the analyzed component is also the "hard" orientation in the understanding of Solas et al. Here, we do not apply any direct recrystallization modeling. In addition, op. cit. deals with static recrystallization

occurring during the post-deformation annealing. However, as long as the conclusions drawn there are correct, the most probable reason behind the disappearance of the $\langle 0001 \rangle \| ED$ maximum seems to be the discontinuous dynamic recrystallization. This does not mean that dynamic recrystallization does not lead to other phenomena important for texture evolution. Detailed investigation of the effect of dynamic recrystallization on microstructure evolution is, however, outside the scope of the present paper.

As the paper presents the optimization of material parameters by comparing only the simulated texture, it is interesting to investigate the sensitivity of the approach to different parameter values. This issue was investigated in the Electronic Supplementary Material. It was revealed that the proposed fitness function is sensitive to such parameters as τ_0, τ_{sat}, f_{sat} and μ, so they could be identified with a good accuracy. On the other hand, it is not much sensitive to β, h_0 and latent hardening parameters. Therefore, to assess the accuracy of these parameters more experimental data would be necessary. To this end the proposed fitness function can be also combined with the classically used functions based on mechanical testing, cf. e.g., Reference 3.

It should be acknowledged that approximating the HE simulation as a simple extrusion is highly simplified. However, one should note that in order to perform the EA optimization, the single simulation should be very computationally efficient. Therefore, the uniform VPSC simulation was the best choice here. In the future, one
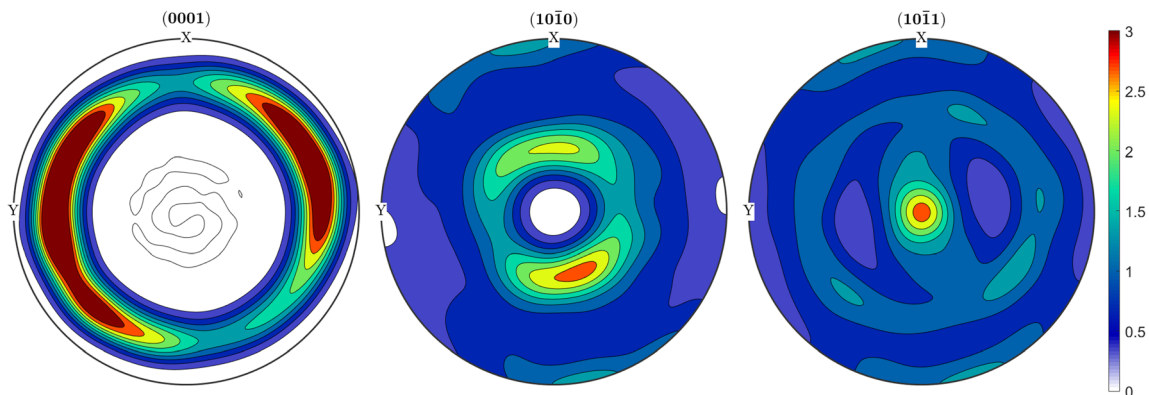

Fig. 12—The simulated texture of Zn-1.5Mg alloy after 1.0 strain (one HE pass) with disabled twinning. The pole figures were plotted using the MTEX[24] software. ED is normal to the plane of the image.
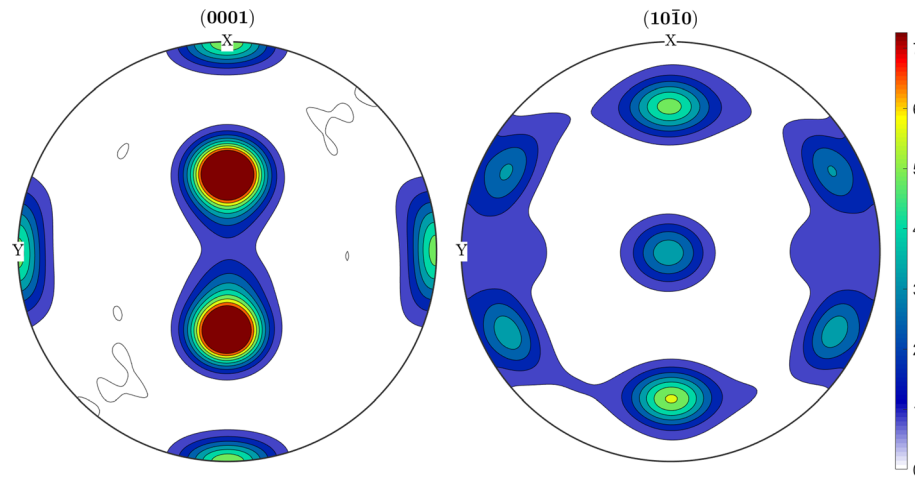
Fig. 13—The simulated texture of pure zinc subjected to rolling with 93 pct thickness reduction as in Ref. 16. The pole figures were plotted using the MTEX[24] software.

can use the obtained set of parameters in order to simulate the whole process using *e.g.*, the finite element method.

It would be interesting to validate the optimized sets of parameters by simulating other plastic deformation process. However, a true validation was not possible due to lack of additional experimental data for the investigated materials of precisely the same composition and deformation history. Nevertheless, we have simulated rolling of pure zinc with the same amount of strain as in Reference 16 and compared the resulting texture (Figure 13) with the experimental one as presented in Figure 6(d) in *op. cit*. Reasonable agreement between the simulated and experimental textures has been found.

VII. CONCLUSIONS

In the paper, the evolutionary algorithm supplied with a newly developed texture-based fitness function was applied in order to establish the crystal plasticity parameters of pure Zn and Zn-1.5Mg alloy subjected to hydrostatic extrusion. The active deformation modes were thus revealed and discussed. It was shown that the predicted slip and twinning system activities are consistent with Schmid factors calculated based on EBSD measurements. In addition to the best of the authors knowledge, this is the first study where the texture evolution of pure Zn with as much as 3.6 strain (4 HE passes) was simulated and where the reorientation due to $\{10\bar{1}2\}\langle10\bar{1}1\rangle$ compressive twinning was taken into account.

Based on the acquired results, it can be concluded that:

– The EA optimization with the fitness function based on numerical texture comparison is a viable tool to obtain the hardening parameters of the VPSC model of pure zinc and zinc-magnesium alloy.

– The basal $\{0001\}\langle2\bar{1}\bar{1}0\rangle$ and pyramidal $<c+a>$ $\{11\bar{2}2\}\langle\bar{1}\bar{1}23\rangle$ slip systems are the main plastic deformation carriers in Zn and its alloy subjected to HE, but reorientation due to $\{10\bar{1}2\}\langle10\bar{1}1\rangle$ compressive twinning plays an important role in texture evolution of both pure zinc and zinc-magnesium alloy in the course of first HE path.

– The dynamic recrystallization (not considered in the applied modeling framework) is partially responsible for some texture evolution effects.

OPEN ACCESS

APPENDIX

The MTEX function for comparing two textures is presented here. The function is called by the Python EA code. Note that the weights are used only for the simulated texture (`fsim`) because the experimental data contains equally weighted orientations.

```
function NTID = compare(fexp,fsim)
    CS = crystalSymmetry('6/mmm',[1.0 1.0 1.856]);
    ori1 = orientation.load(fexp,'columnNames',{'phi1','Phi','phi2'},CS);
    odf1 = calcDensity(ori1);
    ori2 = orientation.load(fsim,'columnNames',{'phi1','Phi','phi2'},CS);
    A = importdata(fsim,' ',0);
    w = A(:,4);
    odf2 = calcDensity(ori2,'weights',w);
    dodf = odf2 - odf1;
    NTID = textureindex(dodf)/textureindex(odf1);
end
```

SUPPLEMENTARY INFORMATION

The online version contains supplementary material available at https://doi.org/10.1007/s11661-021-06285-7.

REFERENCES

1. K. Kowalczyk-Gajewska, K. Sztwiertnia, J. Kawałko, K. Wierzbanowski, K. Wronski, K. Frydrych, S. Stupkiewicz, and H. Petryk: *Mater. Sci. Eng. A*, 2015, vol. 637, pp. 251–63, https://doi.org/10.1016/j.msea.2015.04.040.
2. K. Frydrych and K. Kowalczyk-Gajewska: *Metall. Mater. Trans. A*, 2018, vol. 49A, pp. 3610–23, https://doi.org/10.1007/s11661-018-4676-2.
3. K. Frydrych, M. Maj, L. Urbański, and K. Kowalczyk-Gajewska: *Mater. Sci. Eng. A*, 2020, vol. 771, pp. 1–14, https://doi.org/10.1016/j.msea.2019.138610.
4. K. Frydrych, K. Kowalczyk-Gajewska, T. Libura, Z. Kowalewski, and M. Maj: *Mater. Sci. Eng. A.*, 2021, https://doi.org/10.1016/j.msea.2021.141152.
5. K. Frydrych, Texture evolution of magnesium alloy AZ31B subjected to severe plastic deformation. Eng. Trans. (In review).
6. J. Singh, S. Mahesh, G. Kumar, P. Pant, D. Srivastava, G. Dey, N. Saibaba, and I. Samajdar: *Metall. Mater. Trans. A*, 2015, vol. 46A, pp. 5058–71.
7. Q. Wang, C. Cochrane, T. Skippon, Z. Wang, H. Abdolvand, and M.R. Daymond: *Int. J. Plast.*, 2019, vol. 124, pp. 133–54.
8. P. Bowen, J. Drelich, and J. Goldman: *Adv. Mater.*, 2013, vol. 25, pp. 2577–82.
9. W. Pachla, S. Przybysz, A. Jarzębska, M. Bieda, K. Sztwiertnia, M. Kulczyk, and J. Skiba: *Bioactive Mater.*, 2021, vol. 6, pp. 26–44.
10. A. Jarzębska, M. Bieda, Ł. Maj, R. Chulist, D. Wojtas, M. Strąg, B. Sułkowski, S. Przybysz, W. Pachla, and K. Sztwiertnia: *Metall. Mater. Trans. A*, 2020, vol. 51, pp. 6784–6796, https://doi.org/10.1007/s11661-020-06032-4.
11. A. Jarzębska, M. Bieda, J. Kawałko, P. Koprowski, K. Sztwiertnia, W. Pachla, and M. Kulczyk: *Mater. Lett.*, 2018, vol. 211, pp. 58–61.
12. A. Jarzębska, M. Bieda, J. Kawałko, P. Koprowski, Ł. Rogal, R. Chulist, B. Kania, K. Sztwiertnia, W. Pachla, and M. Kulczyk: in: IOP Conference Series: Materials Science and Engineering, Vol. 375 (IOP Publishing, 2018), p. 012008.
13. L. Cauvin, B. Raghavan, S. Bouvier, X. Wang, and F. Meraghni: *Mater. Sci. Eng. A*, 2018, vol. 729, pp. 106–18.
14. M. Luo and G. Rousselier: *Int. J. Plast.*, 2014, vol. 53, pp. 66–89.
15. D.E. Solas, C.N. Tomé, O. Engler, and H.R. Wenk: *Acta Mater.*, 2001, vol. 49, pp. 3791–3801.
16. R. Parisot, S. Forest, A. Pineau, F. Grillon, X. Demonet, and J.-M. Mataigne: *Metall. Mater. Trans. A*, 2004, vol. 35A, pp. 797–811.
17. O. Casals and S. Forest: *Comput. Mater. Sci.*, 2009, vol. 45, pp. 774–82.
18. J.W. Christian and S. Mahajan: *Prog. Mater. Sci.*, 1995, vol. 39, pp. 1–157.
19. T. Skippon, C. Mareau, and M.R. Daymond: *J. Appl. Crystallogr.*, 2012, vol. 45, pp. 627–43.
20. K. Frydrych: Modelling of microstructure evolution of high specific strength metals subjected to severe plastic deformation processes., Ph.D. thesis, Institute of Fundamental Technological Research, Polish Academy of Sciences, Warsaw, Poland, 2017, (in Polish). https://doi.org/10.13140/RG.2.2.32354.56008.
21. G. Girard, K. Frydrych, K. Kowalczyk-Gajewska, M. Martiny, and S. Mercier: *Mech. Mater.*, 2021, https://doi.org/10.1016/j.mechmat.2020.103685.
22. V.M. Miller, S.L. Semiatin, C. Szczepanski, and A.L. Pilchak: *Metall. Mater. Trans. A*, 2018, vol. 49A, pp. 3624–36.
23. K. Topolski, W. Pachla, and H. Garbacz: *J. Mater. Sci.*, 2013, vol. 48, pp. 4543–48.
24. F. Bachmann, R. Hielscher, and H. Schaeben: in: Texture and Anisotropy of Polycrystals III, Vol. 160 of Solid State Phenomena (Trans Tech Publications Ltd, 2010), pp. 63–68.
25. G.Y. Chin, W.F. Hosford, and D.R. Mendorf: *Proc. R. Soc. A*, 1969, vol. 309, pp. 433–56.
26. P. Van Houtte: *Acta Metall.*, 1978, vol. 26, pp. 591–604, https://doi.org/10.1016/0001-6160(78)90111-6.
27. M.S. Szczerba, T. Bajor, and T. Tokarski: *Philos. Mag.*, 2004, vol. 84, pp. 481–502.
28. A. Molinari, G.R. Canova, and S. Ahzi: *Acta Metall.*, 1987, vol. 35, pp. 2983–94, https://doi.org/10.1016/0001-6160(87)90297-5.
29. R.A. Lebensohn and C.N. Tomé: *Acta Metall. Mater.*, 1993, vol. 41, pp. 2611–24, https://doi.org/10.1016/0956-7151(93)90130-K.
30. C.N. Tomé and R.A. Lebensohn: Manual for Code Visco-Plastic Self-Consistent (VPSC). Version 7b, Technical representation, Los Alamos National Laboratory (2007).
31. K. Kowalczyk-Gajewska: *Eur. J. Mech. Solids A*, 2010, vol. 29, pp. 28–41, https://doi.org/10.1016/j.euromechsol.2009.07.002.
32. K. Kowalczyk-Gajewska: *IFTR Rep.*, 2011, vol. 1, pp. 1–299.

33. J. Arabas: Wykłady z algorytmów ewolucyjnych. (Lectures on evolutionary algorithms), Wydawnictwa Naukowo-Techniczne (2004), (in Polish).
34. M.W. Gutowski: Biology, physics, small worlds and genetic algorithms, Leading Edge Computer Science Research, Nova Science Publishers, Inc. pp. 165–218 (2005).
35. R. Hielscher and H. Schaeben: *J. Appl. Crystallogr.*, 2008, vol. 41, pp. 1024–37, https://doi.org/10.1107/S0021889808030112.
36. B. Beausir and J.J. Fundenberger: ATEX-software, Analysis Tools for Electron and X-ray Diffraction. http://atex-software.eu/.